Computational and Experimental Study of Coumarin-Doped BTCC Crystals for Optical Applications

Andersen H.M. & El-Farouk A.R.

Department of Ophthalmic Research, Copenhagen Medical Institute, Copenhagen, Denmark
Department of Clinical Vision Sciences, Cairo Biomedical University, Cairo, Egypt

ABSTRACT

In the present investigation, Pure and Coumarin doped BTCC crystals were grown by slow evaporation technique at room temperature. Grown crystals have been characterized using single crystal X-ray diffraction, Fourier Transform Infrared Spectroscopy (FTIR), Thermal, UV- visible spectroscopy and NLO studies. The presences of dye were confirmed by FTIR and XRD spectra. The natural bond orbital (NBO) analysis was used to study the stability and charge delocalization of the molecule. The HOMO-LUMO energies describe the charge transfer takes place within the molecule. Molecular electrostatic potential has been analyzed. The developments try an extensive scale with this enhanced pH qualities is required to yield mass crystal appropriate for laser combination tests and SHG device applications.

Keywords: *Crystal Growth, BTCC crystal, FT-IR studies, Thermal studies, HOMO-LUMO studies, SHG measurements.*

I. INTRODUCTION

During the last few decades, organic materials have been of particular interest because the nonlinear optical responses in this broad class of materials is microscopic in origin, offering an opportunity to use theoretical modeling coupled with synthetic flexibility to design and produce novel materials[1-4].Semiorganic nonlinear optical materials are receiving a great deal of attention, as they have large optical susceptibilities, inherent ultra fast response times and high optical thresholds for laser power compared with inorganic materials. BTCC has been reported as a promising organic NLO material, which has SHG efficiency three times higher than KDP [5]. In order to improve the physicochemical properties attempts have been made to incorporate metal dopants.

In the present investigation, a systematic study has been carried out on the growth of pure and Coumarin doped BTCC crystals. Powder X-ray diffraction studies were carried out and the lattice parameters were calculated by least square method for the grown pure and doped crystals. The SHG efficiency of the pure and doped BTCC crystals were also studied using Nd: YAG Q-switched laser. The results of these investigations are discussed in this paper.

II. CRYSTAL GROWTH

The pure and doped BTCC crystals were grown by slow evaporation technique at room temperature (30°C).Within a week time, transparent seed crystals were formed due to spontaneous nucleation and among them tiny crystals with perfect shapes were used for growth experiments. Figure 1 shows the photograph of grown pure and doped crystals of BTCC with dimensions of $17\times13\times9mm^3$ and $11\times7\times5mm^3$, grown in a period of 17 and 21 days respectively. The crystals are found to be highly transparent, free from visible inclusions and non-hygroscopic in nature. Interestingly, microbial growth was not observed during the entire growth period and even after two months [6].

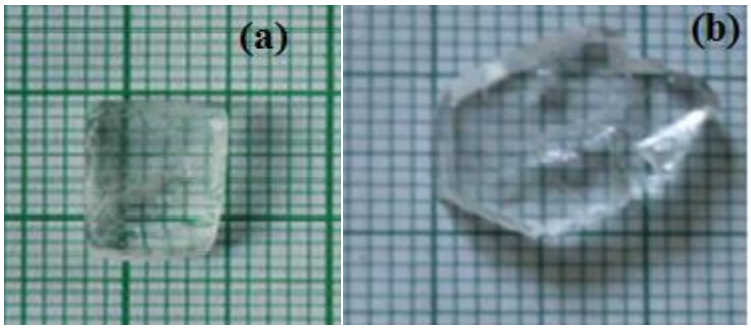

Figure 1. Photograph of as grown crystals of pure and Coumarin doped BTCC crystal

III. RESUTLS AND DISCUSSION

3.1 Powder XRD Studies

The structural properties of single crystals of pure and doped BTCC have been studied by X-ray powder diffraction technique [7]. Powder X-ray diffraction studies of pure and doped BTCC crystals were carried out, using Rich Seifert XRD 3000P, X-ray diffractometer with Cu K_α (λ=1.54056Å) radiation. The samples were scanned for 2θ values from 10˚ to 80˚ at a rate of 2˚ /min. Figure 2 shows the Powder XRD pattern of the pure and doped BTCC crystal. The diffraction patterns of the pure and doped BTCC crystals have been indexed by least square fit method. The lattice parameter values of the pure and doped BTCC crystal has been calculated and is well matched with the reported literature. It is seen that both the pure and doped crystals crystallizes variations in the lattice parameters which are due to the incorporation of the dopant in the BTCC crystal lattice.

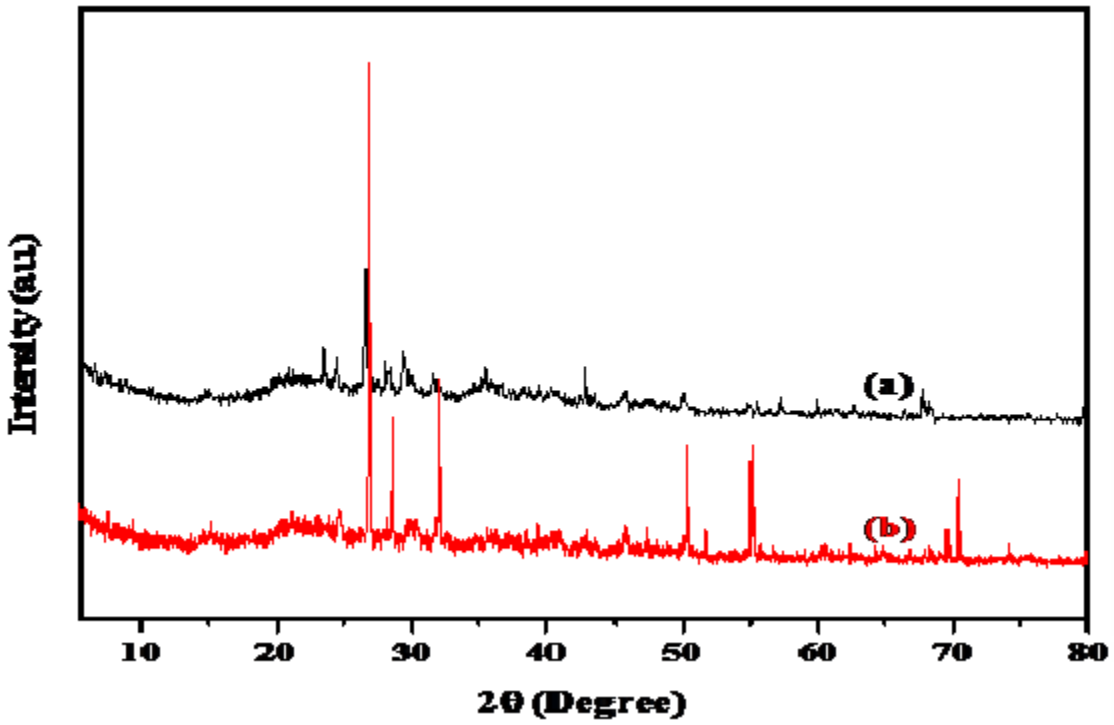

Figure 2. Powder XRD pattern of (a) pure and (b) Coumarin doped BTCC crystal

3.2. FT-IR Analysis

The FT-IR spectrum was recorded between 500 cm^{-1} and 4000 cm^{-1}, using BRUKER IFS 66V FT-IR spectrometer. The FT-IR spectra of pure and doped BTCC appear almost similar to each other. N-H stretching frequencies of amino group are found between 3812 cm^{-1} and 2600 cm^{-1} for both pure and doped crystals [8]. Both the pure and doped compounds show absorption at 1620 cm^{-1} indicating the presence of primary amino group. The characteristic absorption for the -NH group in the aromatic ring is observed at 1310 cm^{-1} for BTCC. The broad absorption around

3000 cm^{-1} indicates the co presence of C=O stretching and O-H stretching. The FT-IR spectra of both the pure and doped BTCC confirm the structural aspects [9]. Doping of metal ion into the crystal lattices does not show any significance change in absorption pattern. Some of the absorptions show a marked difference in percentage transmittance. The percentage change of transmittance especially, at 950 cm^{-1} and 690 cm^{-1} are worth noting. It is inferred that the metal ion, form weak linkages in the interstices of the corresponding crystals.

The polarized FTIR spectra were recorded for the pure and doped BTCC in order to qualitatively analyze the presence of functional groups in BTCC, in the range 50 cm^{-1} – 3500 cm^{-1}. The recorded spectra of the pure and doped BTCC are shown in Figure 3. The characteristic peaks observed for zwitter ions of amino acids are present in the FTIR spectra of BTCC [10]. The peak at 2686.4 cm^{-1} is for O-H stretching of carboxylic group. The N-H stretching of amino group is observed as a weak absorption at 3130 cm^{-1}. The peaks at 1199.53 cm^{-1}, 1417 cm^{-1} and 1628 cm^{-1} are for the C=O stretching of carboxylic group. The absence of peak at 1818 cm^{-1} in the dye.BTCC may be due to the metal linkage with the N of amino group.

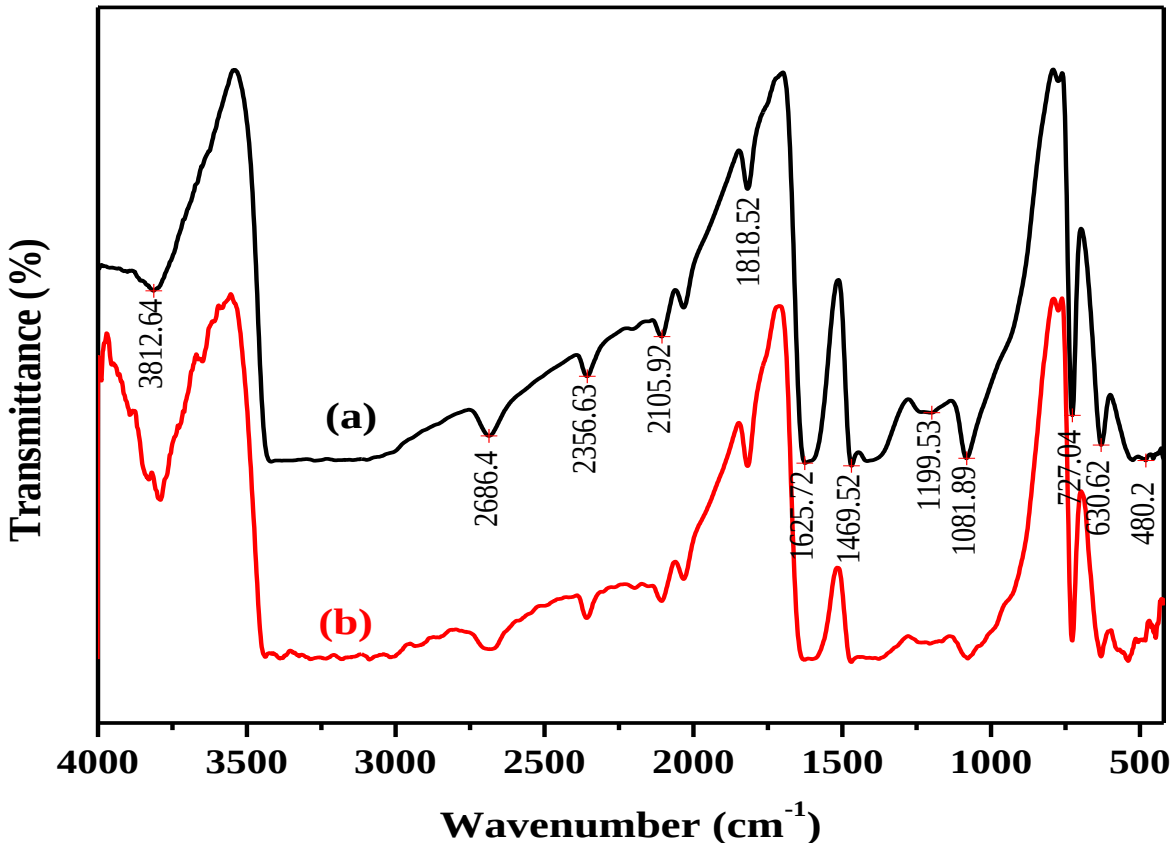

Figure 3. FT-IR spectra of pure and Coumarin doped BTCC crystal

3.3. Microhardness Studies

Microhardness studies have been carried out on pure and doped BTCC crystal using HMV SHIMADZU Vickers microhardness tester fitted with a Vickers diamond pyramidal indenter attached to an incident light microscope [11]. The static indentations were made at room temperature with a constant indentation time of 15 seconds for all indentations. The indentation marks were made on the polished faces of the sample by varying the load from 5 g to 25 g. Beyond this load the formation of micro cracks were observed, hence readings were not taken for higher loads. The Vickers microhardness was evaluated for the face (0 1 0) of the pure and doped BTCC crystals [12]. Vickers microhardness profile as a function of the applied test loads is illustrated in Figure 4. The decrease of the microhardness with the increasing load is in agreement with the normal indentation size effect (ISE).

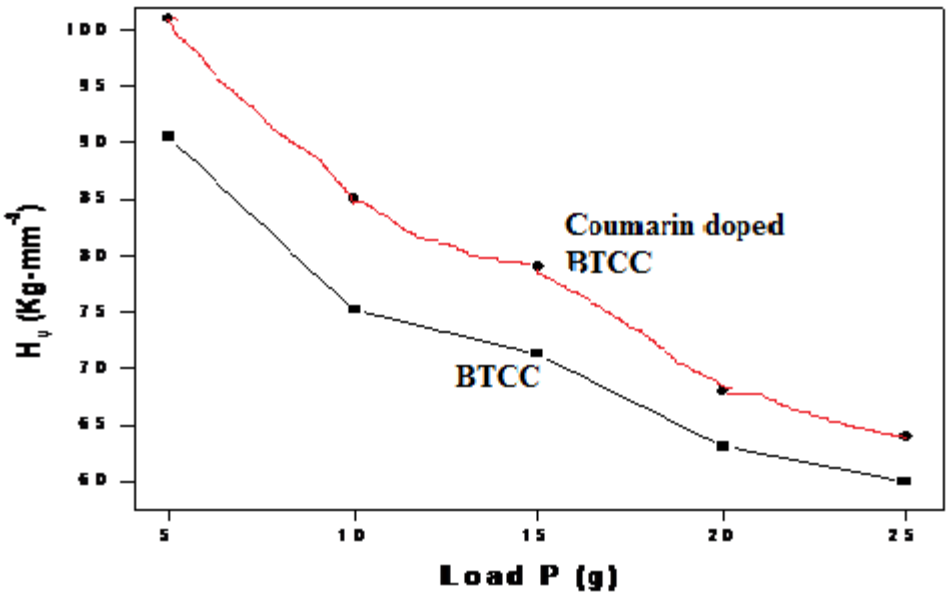

Figure 4. Variation of Hv with load for pure and Coumarin doped BTCC crystal

3.4. Thermal Studies

The TGA and DTG analysis of BTCC were carried out in nitrogen atmosphere from 28°C -1200 °C, using the instrument NETSZCH STA 409C. Figure. 5 shows the TGA and DTG thermograms of pure and doped BTCC. The first weight loss of about 35% observed in BTCC starts at 115°C could be attributed to the loss of lattice water. The next stage between 115.5°C with a total loss of 59% is assigned to the decomposition of BTCC. The resulting residue gives a weight loss for a wider range of temperature between 330°C and 1000°C. TG analysis of the doped BTCC shows that the softening starts at 114.9˚C due to loss of water. There is a slight reduction in the decomposition temperature of the doped crystals compared to the pure BTCC crystal [13].

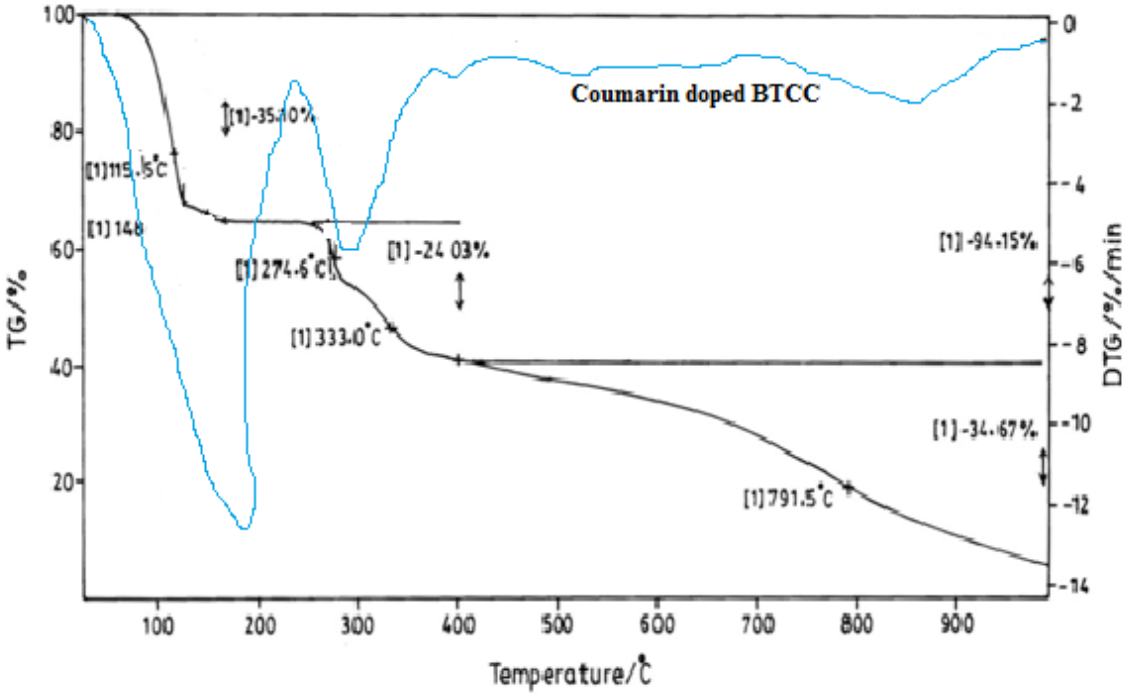

Figure 5. TGA and DTG curves of pure and Coumarin doped BTCC crystal

The reduction in the decomposition temperature is due to the decreased bond energy caused by the addition of dye. The TG analysis coincides well with the DTG thermogram.

3.5 DFT Studies on coumarin doped BTCC crystal

The TD-DFT/6-31G [1] calculations involving configuration interaction between the singly excited electronic states were performed in the gaseous phase and in the ethanol solution (IEF-PCM model). Both the frontier molecular orbitals, highest occupied molecular orbital (HOMO) and lowest unoccupied molecular are the main orbitals taking part in chemical reaction [14]. The electron delocalization between HOMO and LUMO is the principal factor in determining the easiness of a chemical reaction and the stereoselective path, irrespective of intra- and intermolecular process; therefore, they are the most important orbitals which help in determining the way molecule interacts with other species. The TD-DFT was employed for obtaining these FMOs. The electronic transition corresponds from HOMO (characterizes of electron giving) to the LUMO (characterizes of electron accepting) orbital [15-17].

To understand the electronic transitions, positions of experimental absorption peaks, calculated wavelengths (λmax), vertical excitation energies, oscillator strengths (f), dipole moments, and excitation transition and solvent environment are carried out in Table 1. The energy gap between the HOMO and LUMO molecular orbitals characterizes the chemical reactivity and kinetic stability along with spectroscopic properties. There was a difference observed in the transition orbitals on going from gaseous to solvent phase. The values for comparison are tabulated in the Table 1. From the Fig. 6 (of solvent phase) and Fig. 7 (of gaseous phase), it was clearly visible that in LUMO the charge was mainly accumulated on the C=C parts of the rings, on the nitro group both in case of isolated atom and solvent.

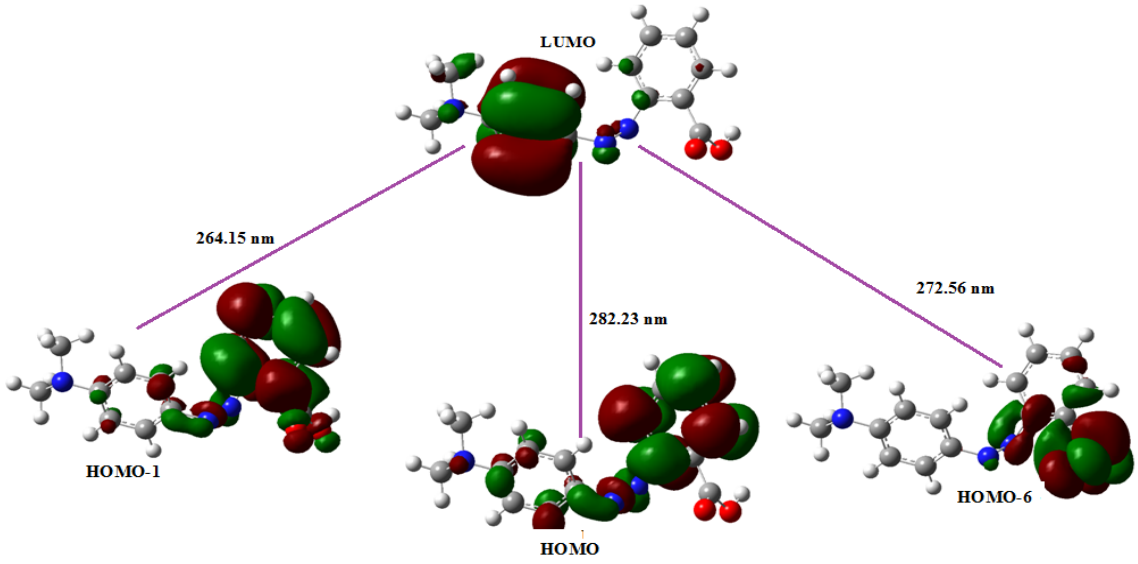

Figure 6. Plot of HOMO LUMO surfaces along with the energy gaps in BTCC

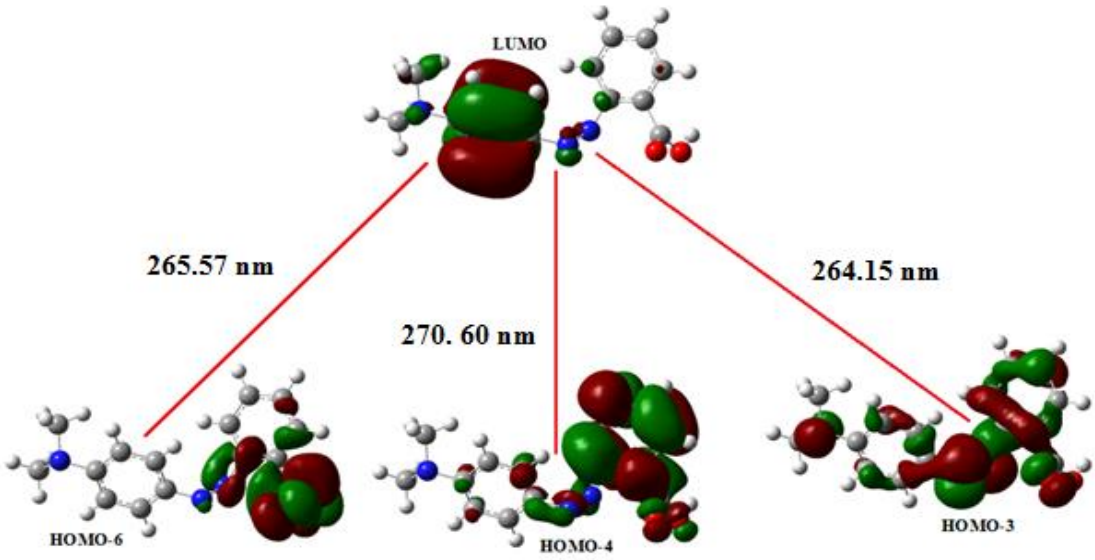

Figure 7.HOMO LUMO surfaces along with energy gaps in Isolated Gaseous phase.

3.5.1 Electronic absorption and Frontier Molecular orbitals (FMOs)

However, in case of isolated gaseous phase in HOMO and HOMO-1 charge density along with ring is visible on the methyl group, on the O atoms and on the nitro group. In HOMO-6 it was shifted from dichloroacetamide to the hydrocarbon chain. But as far as solvent is concerned in case of HOMO-6 and HOMO-4 the charge was shifted from the ring to the hydrocarbon chain with some portions on the methyl group, whereas in HOMO-3 the whole charge was concentrated on the ring[18]. These plots give an idea about the charge concentrations and the changes in them when dissolved in solvent. The band gap and dipole moment was also calculated for gaseous and solvent (ethanol) phase as reported in Table 1.

3.5.2 Molecular Electrostatic Potential (MEP).

Developing an ability to predict the structure and structure–property relations of conducting molecule in the bulk will assist the design of new structures that combine processability with favourable electronic properties [19]. The molecular electrostatic potential (MEP) at a given point r(x,y,z) in the vicinity of a molecule can be defined as the force acting on a positive test charge (a proton) located at 'r' through the electrical charge cloud generated through the molecules, electrons and nuclei and given by the expression

$$V(r) = \sum Z_A / |R_A - r| - \int \rho(r') / |r' - r| \, dr'$$

where ZA is the charge on nucleus A located at RA and F (r′) is the electronic density. The first term in the expression represents the effect of the nuclei and the second represents that of electrons. MEP of a molecule has always proved to be a good guide in assessing the molecules reactivity towards positively or negatively charged reactants despite of the fact that the molecular charge distribution remains unperturbed through the external test charge (no polarization occurs). Also it is observed that there is a strong correlation of dipole moment, electronegativity, and partial charges with electrostatic potential and by utilizing quantum mechanical calculations values could be generated for partial charges for the atoms in a molecule.

Electronegativity of atoms in molecules indicates where partial charges are likely to be found - the most electronegative atoms are most negative, the others are less negative or more positive. The greater the difference in partial charges, the more polar the molecule. The MEP provides a visual method to understand the relative polarity of a molecule through mapping total density surface on electrostatic potential energy surface. Such surfaces depict the size, shape, charge density, and site of chemical reactivity of the molecules. In the surface generated negative electrostatic potential corresponds to an attraction of the proton by the concentrated electron density in the molecules (from lone pairs, pi-bonds, etc.) (Colored in shades of red) and positive electrostatic potential corresponds

to repulsion of the proton by the atomic nuclei in regions where low electron density exists and the nuclear charge is incompletely shielded (colored in shades of blue). If the surface is largely white or lightercolor shades, the molecule is mostly non-polar. Potential increases in the order red < orange < yellow < green < blue. Here we have presented the MEPs with the help of Gauss View programme.

The plot of electrostatic potential surface mapped on electron density isosurface is shown in Figure 8 for hexamer of BTCC + DYE. The MEP shows that the highest negative potential visible as red blob is localized over the middle region of the two benzene rings and in the middle of the rings. Also a less negative area reflected as a yellowish blob is visible near the surrounding regions of the red portions. A very weak positive charge is localized over the above portions of the fulvene ring and could be observed as little bluish regions.

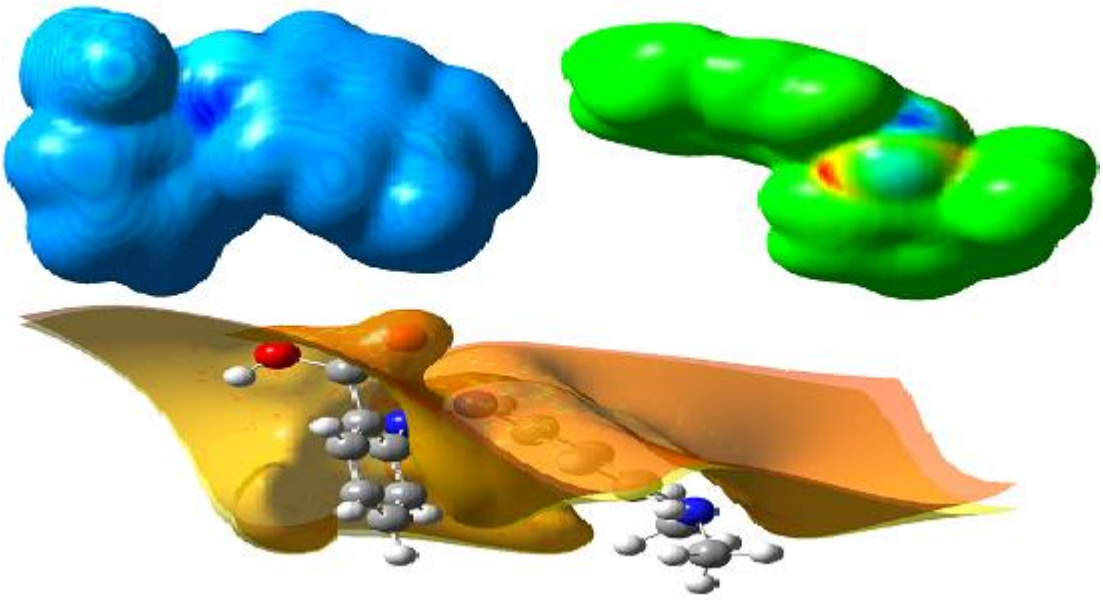

Figure 8. The molecular electrostatic potential surface of Coumarin doped BTCC

3.5.3 Thermodynamic Properties

The importance of computation of thermodynamic properties of molecules lies in thermochemistry and chemical equilibrium. The equations utilized for computing thermochemical data in Gaussian programs are derived from statistical thermodynamics with the two key ideas, the Boltzmann distribution and the partition function[20]. The equations utilized in those programs are given in statistical mechanics texts . The partition function is like a thermodynamic wave function, in the sense that it contains all thermodynamic information about the system, just as the quantum mechanical wave function contains all dynamic information. The total energy, zero point energy, rotational constants, dipole moment, heat capacity ($C^{o}p,m$), entropy($S^{o}m$) and enthalpy($H^{o}m$) of the CPP was directly obtained from the output of Gaussian programs in the optimization and vibration calculations. It was observed that the values of $C^{o}p,m$, $S^{o}m$ and $H^{o}m$ increases with increase in temperature from 100 K to 500 K because the molecular vibrational intensities are increasing with temperature. The correlation between temperature and these thermodynamic properties are given in Figure 9. The correlation equations are as follows:

$C^{o}p,m = 34.30589+0.38303T+2.69434*10\text{-}5T2$ (R2=0.99957)

$S^{o}m = 97.16984+0.68186T-0.00025T2$ (R2=0.99971)

$H^{o}m = 419.01489+0.0302T+0.0002T2$ (R2=1)

These equations could be utilized in predicting the Gibbs free energy which helps when the form A is to be differentiated from the biologically active form B. Also it would help in the judgement of spontaneity of the reactions towards any reactant in which both the form A and form B would be involved. Also, the thermodynamic data would provide useful information for the study of thermodynamic energies and estimate directions of chemical reactions according to the second law of thermodynamics in thermochemical field.

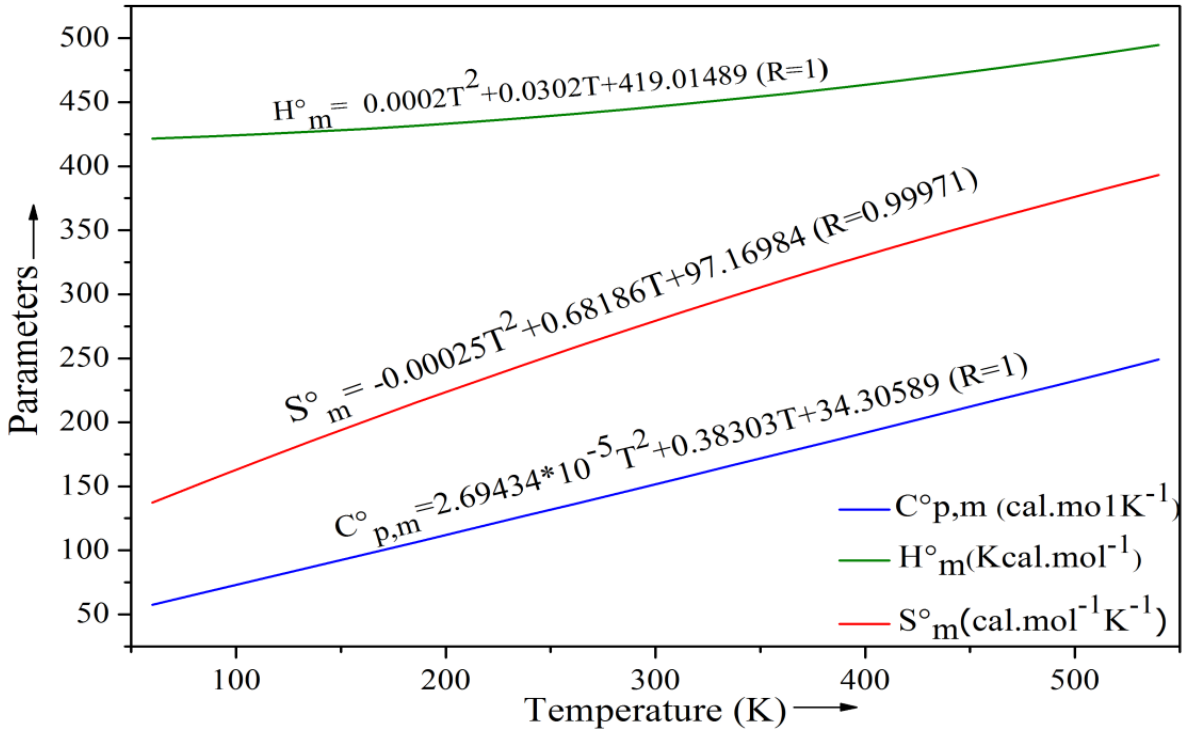

Figure 9. Correlation graphic of heat capacity (C°p,m cal.mo1K-1), enthalpy (H°m Kcal.mol-1), entropy (S°mcal.mol-1K-1) and temperature for Coumarin doped BTCC

3.5.3 Conformational studies

For the identification of all possibilities of rotational isomerism in Coumarin doped BTCC in a 1-D potential energy surface (PES) scan has been performed around Φ(C6-C5-C7-C8) at B3LYP/6-31G level of theory[21]. The PES is the mathematical or graphical relationship between the energy of a molecule (or a collection of molecules) and its geometry. The scan studies were obtained by minimizing the potential energy in all geometrical parameters by varying the torsional angles at a step of 10° in the range of 0-360° rotation around the bond C5-C7. The chemical structure of Coumarin doped BTCC has two functional groups as a substituent, nitro at C11 (para position of the ring) and methyl at C5 (position 2 of the ring). These are two stereogenic centres and allow for four possible stereoisomers. But according to the literature survey, only two N are known to exist at room temperature which was very well elucidated by the double well potential energy curve (Fig. 6). It clearly shows three energy minima at -173.461°, -28.421° and 90.051° with energies -2534.86097, -2534.86006 and -2534.8571 a.u, respectively. Each energy minimum can be associated coumarin doped BTCC; the former well is deeper than the other two and thus it represents the most stable conformation to be called conformer. If we consider the two methyl group as fixed, then the ring is in trans conformation to the hydrocarbon chain in conformer and in cis conformation in conformer. In The most stable optimized structure was used in the vibrational frequency calculation to characterize all stationary points as minima. Fig. 6 is the ground state optimized structure.

3.6 NLO Studies

The nonlinear property of the grown BTCC crystal was tested by passing the output of Nd: YAG Quanta ray laser emitting 1064 nm, generating about 6 mJ per pulse. The details of the experimental set-up are already discussed in previous Chapters. The input laser beam was passed through an IR reflector and then directed on the microcrystalline powdered sample packed in a capillary tube of diameter 0.154 mm. The light emitted by the sample was detected by photodiode detector and oscilloscope assembly. The SHG efficiency of BTCC was determined by Kurtz and Perry powder technique. Microcrystalline materials of KDP were used for comparison with BTCC for Second Harmonic Generation experiments. For a laser input of 6.2mJ, the second harmonic signal (532nm) of 91.66mW, 272.12mW and 438.39mW were obtained for, pure KDP and coumarin doped BTCC respectively. The SHG efficiencies of pure and doped crystals are 3 and 4.7 times respectively higher that of KDP. Thus, the coumarin has increased the efficiency of pure BTCC.

IV. CONCLUSION

Good quality single crystals of pure and doped BTCC were grown successfully by slow evaporation technique. Powder X-ray diffraction studies were carried out, and the lattice parameters are calculated. Inductively coupled plasma studies shows that the amount of dopant incorporated into the doped crystal is less than the concentration of the dopant in the corresponding solution. The pure and doped BTCC crystals are transparent in the entire visible region, and have minimum absorption. The TGA and DTG studies show that the metal dopants have not altered the thermal stability of the molecules. Hardness studies show that pure and doped KDP crystals are soft materials. NLO studies proved that the metal dopant have increased the efficiency of pure KDP. The presence of dopant has improved the Nonlinear optical (NLO) properties of the grown crystals and these crystals can be promising material for nonlinear device fabrication.

REFERENCES

1. *L.F. Warren, in: R.E. Allred, R.J. Martinez, K.B. Wischmann (Eds.), Electronic Material, Society for the Advancement of Material and Process Engineering, Covina, CA, 1990, p. 388.*
2. *P.R. Newman, L.F. Warren, P. Cunningham, T.Y. Chang, D.E. Copper, G.L. Burdge, P. Polak Dingels, C.K. Lowe-Ma, in: C.Y. Chiang, P.M. Chaikan, D.O. Cowan (Eds.), Advanced Organic Solid State Materials, Vol. 173, 370.*
3. *P. Kerkoc, V. Venkataraman, S. Lochran, R.T. Bailey, F.R. Cruickshank, D. Pugh, J.N. Sherwood, J. Appl. Phys. 80(1996) 6666*
4. *Pricilla Jeyakumari, J. Ramajothi, S. Dhanuskodi, J. Cryst. Growth 269, 558-564 (2004).*
5. *Kuppusamy Sambathkumar, Spectrochim. Acta A , 2015(147)51-66.*
6. *K. Sambathkumar, S. Nithiyanantham, J Mater Sci: Mater Electron,2017; (28):6529-6543.*
7. *R. Rajesekaran, P.M. Ushasree, R. Jayavel, P. Ramasamy, J. Cryst. Growth 229 (2001) 563.*
8. *M. Oussaid, P. Becker, C.C. Nedelec, Phys. Stat. Sol. (b) 207 (1998) 499.*
9. *G. Xing, M. Jiang, Z. Sao, D. Xu, Chin. J. Lasers 14 (1987)302.*
10. *V. Venkataramanan, C.K. Subramanian, H.L. Bhat, J. Appl. Phys. 77 (1995) 6049.*
11. *N.R. Dhumane, S.S. Hussaini, V.V. Nawarkhele, M.D. Shirsat, Cryst. Res. Technol 41, 897-901 (2006).*
12. *S. Selvakumar, J. Packiam Julius, S.A. Rajasekar, A. Ramanand, P. Sagayaraj, Mater. Chem. Phys. 89, 244-248 (2005).*
13. *V. Venkataramanan, C.K. Subramanian, H.L. Bhat, J. Appl. Phys. 77, 6049-6051 (1995).*
14. *N.R. Dhumane, S.S. Hussaini, Kunal Datta, Prasanta Ghosh and Mahendra D. Shirsat, J. Pure Appl. & Ind. Phys. Vol.1 (1), 45-52 (2010).*
15. *B. Latha , P. Kumaresan, S. Nithiyanantham , K. Sambathkumar, Journal of Molecular Structure, 2017 (1142)255-257.*
16. *P.A. Angeli Mary, S. Dhanuskodi, Cryst. Res. Technol. 13(36) (2001) 1231.*
17. *S.B. Monaco, L.E. Davis, S.P. Velsko, F.T. Wang, D.Eimerl, A. Zalkin, J. Cryst. Growth 85 (1987) 252.*
18. *X.Q. Wang, D. Xu, M.K. Lu, D.R. Yuan, S.X. Xu, Mater. Res. Bull. 36 (2001) 879.*
19. *S. Velsko, Laser Program Annual Report, Lawrence UCRL-JC 105000, Lawrence Livermore National Laboratory, Livermore, CA, 1990.*
20. *P.M. Ushashree, R. Jayavel, C. Subramanian, P. Ramasamy, Bull. Electrochem. 14 (1998) 407.*
21. *P.M. Ushashree, R. Jayavel, Optical Materials 21 (2002) 599–604.*